Quasilinear treatment of wave-particle interactions in the electron cyclotron range and its implementation in a gyrokinetic code

P. Donnel, J. Cazabonne, L. Villard, S. Brunner, S. Coda, J. Decker, M. Murugappan, M. Sadr

École Polytechnique Fédérale de Lausanne (EPFL), Swiss Plasma Center (SPC), CH-1015 Lausanne, Switzerland

E-mail: peter.donnel@epfl.ch

Abstract. A quasilinear operator for wave-particle interactions in the electron cyclotron range is derived using the cold plasma dispersion relation. The finite width of the beam implies a broadening of the resonance layer in the velocity space which allows the use of a numerically efficient treatment of the operator. The specific case of a pure heating injected at the outer mid-plane is then treated. It allows to treat the beam propagation and absorption easily, simplifying the implementation of the source term in the gyrokinetic code. This specific case is implemented in the gyrokinetic PIC code ORB5 using a Langevin approach. The derivation and verification of the source operator are presented.

1. Introduction

One of the main mechanisms to heat a hot plasma is to send a wave that will transfer its energy to particles via wave-particle interaction. For an efficient coupling of the wave with the plasma, resonant processes are needed, implying that the wave frequency is a multiple of the cyclotron frequency of one of the species present in the plasma. When the beam frequency is in the electron cyclotron (EC) range, the beam deposits its energy on electrons. This process can be used to heat the plasma or to generate a current. One of the advantages of using an EC beam is that the spatial deposition of the power is narrow, which allows controlling MHD instabilities [1].

It has been experimentally observed that the area of deposition of an EC beam can be wider than expected, potentially leading to inaccurate power deposition [2]. Two mechanisms have been proposed to explain this observation. The first option is the scattering of the beam by turbulent fluctuations essentially at the edge [3]. This mechanism has been numerically and experimentally tested in the toroidal device TORPEX and the tokamak TCV for transmitted EC waves using a full-wave beam propagation code in presence of turbulent fluctuations [4, 5]. It has been shown in TCV that density fluctuations in the Scrape-Off Layer lead to instantaneous fluctuations of the transmitted beam power profile consistent with experimental observations. These instantaneous fluctuations tend to broaden the beam on average. This effect is expected to be significant in ITER, where the beam will have to travel over a longer path before reaching the resonance than in today's tokamaks [6]. The second proposed mechanism suggests that the heating due to the power deposition leads to

a locally enhanced radial transport of particles. This mechanism has been tested by coupling a beam propagation code (Ray Tracing) with a local Fokker-Planck code and by adding an *ad hoc* transport term [7, 8, 9]. Especially, it has been shown in [9] that this *ad hoc* transport needs to be localised both in position and velocity spaces where the wave-particle interaction takes place to match Hard X-Ray measurements from suprathermal electron Bremsstrahlung emission. To study this problem on a first-principle basis, the coupling of a global flux-driven gyrokinetic code with a wave propagation code is an appropriate tool.

Different global flux-driven gyrokinetic codes have been developed in the last two decades. To the authors knowledge, all of these codes are using simplified source terms [10, 11, 12, 13], able to sustain profiles for long simulations but too simple to study in detail the effect of the source on transport. The implementation of a realistic source in a flux-driven gyrokinetic code will therefore enable the study of different physical problems related to the modification of transport by the presence of the source. In this paper, the implementation of a realistic EC source in a flux-driven gyrokinetic source is reported for the first time.

The rest of this article is organised as follow. In part 2, the general form of quasi-linear operators for wave-particle interactions is presented in the specific case of a uniform and constant magnetic plasma. In part 3, the specific case of a beam with a frequency in the EC range is treated. In part 4, the resonance broadening due to the finite width of the beam is treated analytically. To ease the first implementation of this source in the gyrokinetic code, the specific case of a pure heating beam propagating along the mid-plane is detailed in part 5. In part 6, the numerical scheme for the implementation of the source in the ORB5 code is presented. The implementation is verified by investigating several test cases in part 7.

2. Quasi-linear operator for wave-particle interactions

Historically, the quasilinear formalism for the diffusion operator describing the interaction between radio-frequency waves and an infinite and uniform plasma has been developed by Kennel and Engelmann [14]. Relativistic effects have been added to the model by Lerche [15].

We consider an electric field propagating in a plasma. In this paper, a monochromatic wave of pulsation ω_b is considered. This electric field in real space can be represented as a Fourier transformation from the corresponding Fourier description

$$\mathbf{E}(\mathbf{x},t) = \int \frac{d^3k}{(2\pi)^3} \int \frac{d\omega}{2\pi} e^{i\mathbf{k}\cdot\mathbf{x}-i\omega t} \mathbf{E}_{\mathbf{k}}(\mathbf{k},\omega) \left[\delta(\omega-\omega_b) + \delta(\omega+\omega_b)\right]. \tag{1}$$

In this expression, $\mathbf{k}$ is the wave vector and $\mathbf{E}_{\mathbf{k}}$ the component of the electric field associated with $\mathbf{k}$. The propagation of this electric field leads to a plasma-wave interaction that can be represented by a quasilinear operator. The quasilinear operator for the general case of a uniform plasma immersed in a constant and uniform magnetic field $\mathbf{B}_0$ is given by

$$\frac{\partial F}{\partial t} = Q = \sum_{n=-\infty}^{+\infty} Q_n \tag{2}$$

where F is the distribution function of the species coupling with the beam and n stands for the harmonic considered. Each component Q_n takes the form [16]

$$Q_n = \nabla_{\mathbf{v}} \cdot [\mathbb{D}_n \cdot \nabla_{\mathbf{v}} F] \tag{3}$$

with the diffusion matrix defined as

$$\mathbb{D}_n = \lim_{V\to 0} \frac{1}{V}\frac{\pi}{2}\frac{Z^2e^2}{m^2}\int \frac{d^3k}{(2\pi)^3}\int \frac{d\omega}{2\pi}\frac{k_\parallel^2}{\omega^2 v_\perp^2}\delta\left(\omega - k_\parallel v_\parallel - n\omega_c\right)\left|\mathbf{w}_n^{\star T}\mathbf{E}_\mathbf{k}\right|^2 \mathbf{u}_n\mathbf{u}_n^T \times\left[\delta\left(\omega-\omega_b\right)+\delta\left(\omega+\omega_b\right)\right]. \tag{4}$$

In this expression, m, Ze and $\omega_c = \frac{ZeB_0}{m\gamma}$ are respectively the mass, the charge and the relativistic cyclotron frequency (with γ the relativistic Lorentz factor) of the species considered. $k_\parallel$, $k_\perp$ are the parallel and perpendicular components of the wave vector with respect to the magnetic field and V is the volume of integration. The exponents T and $*$ refer respectively to the matrix transpose and to the complex conjugate. The integration over frequencies can be directly performed here, leading to

$$\mathbb{D}_n = \lim_{V\to 0} \frac{1}{V}\pi\frac{Z^2e^2}{m^2}\int \frac{d^3k}{(2\pi)^4}\frac{k_\parallel^2}{\omega_b^2 v_\perp^2}\delta\left(\omega_b - k_\parallel v_\parallel - n\omega_c\right)\left|\mathbf{w}_n^{\star T}\mathbf{E}_\mathbf{k}\right|^2 \mathbf{u}_n\mathbf{u}_n^T. \tag{5}$$

We define a basis $(\mathbf{e}_x, \mathbf{e}_y, \mathbf{e}_z)$ such that $\mathbf{B}_0 = B_0\mathbf{e}_z$ and $\mathbf{k} = k_\perp\mathbf{e}_x + k_\parallel\mathbf{e}_z$. The vector $\mathbf{w}_n$ in Eq.5 is defined in the Cartesian basis $(\mathbf{e}_x, \mathbf{e}_y, \mathbf{e}_z)$ as

$$\mathbf{w}_n = \begin{pmatrix} v_\perp \frac{n}{\rho} J_n(\rho) \\ -iv_\perp J_n'(\rho) \\ v_\parallel J_n(\rho) \end{pmatrix}. \tag{6}$$

In this expression, J_n is the n-th Bessel function of first kind and $\rho = k_\perp v_\perp/\omega_c$ its argument, accounting for Finite Larmor Radius effects. In Eq.5, $\mathbf{u}_n$ represents the direction of the diffusion due to wave-particle interaction which reads in the cylindrical basis $\left(\mathbf{e}_\perp, \mathbf{e}_\parallel\right)$ (Note that $\mathbf{u}_n$ does not have an $\mathbf{e}_\varphi$ component due to the symmetry of the problem).

$$\mathbf{u}_n = \begin{pmatrix} \frac{\omega_b}{k_\parallel} - v_\parallel \\ v_\perp \end{pmatrix}. \tag{7}$$

Using the resonance condition, $\omega_b = k_\parallel v_\parallel + n\omega_c$, one can define the vector $\mathbf{s}_n$ as

$$\mathbf{s}_n = \mathbf{u}_n\frac{k_\parallel}{\omega_b} = \begin{pmatrix} \frac{n\omega_c}{\omega_b} \\ \frac{k_\parallel v_\perp}{\omega_b} \end{pmatrix} = \begin{pmatrix} s_n^\perp \\ s_n^\parallel \end{pmatrix} \tag{8}$$

allowing the simplification of the definition of the diffusion matrix Eq.5 which reads

$$\mathbb{D}_n = D_n\mathbf{s}_n\mathbf{s}_n^T = \begin{pmatrix} D_n^{\perp\perp} & D_n^{\perp\parallel} \\ D_n^{\perp\parallel} & D_n^{\parallel\parallel} \end{pmatrix} \tag{9}$$

with the resonant diffusion coefficient defined as

$$D_n = \pi\frac{Z^2e^2}{m^2}\lim_{V\to 0}\frac{1}{V}\int\frac{d^3k}{(2\pi)^4}\delta\left(\omega_b - k_\parallel v_\parallel - n\omega_c\right)\left|\mathbf{\Pi}_n^{\star T}\mathbf{E}_\mathbf{k}\right|^2. \tag{10}$$

In this expression, $\mathbf{\Pi}_n = \mathbf{w}_n/v_\perp$. Consequently one gets

$$\mathbf{\Pi}_n^{\star T}\mathbf{E}_\mathbf{k} = J_{n-1}(\rho)\frac{E_{\mathbf{k},+}}{\sqrt{2}} + J_{n+1}(\rho)\frac{E_{\mathbf{k},-}}{\sqrt{2}} + \frac{v_\parallel}{v_\perp}J_n(\rho)E_{\mathbf{k},\parallel} \tag{11}$$

where $E_{\mathbf{k},+}$, $E_{\mathbf{k},-}$ are respectively the left- and right-handed polarized electric field components

$$E_{\mathbf{k},\pm} = \frac{E_{\mathbf{k},x} \pm iE_{\mathbf{k},y}}{\sqrt{2}}. \tag{12}$$

3. Plasma-wave interaction in the electron cyclotron range

3.1. Details of interaction with electrons

The quasi-linear operator presented in the part 2 is valid for any species. In the rest of this paper a beam with a typical frequency in the EC range is considered. Hence, only electrons will couple to the beam. Since $\omega_{ce} = -\Omega_e/\gamma < 0$, where $\Omega_e = eB/m_e$ is the non-relativistic absolute value of the electron cyclotron frequency, the resonant condition in Eq.10 implies that the plasma-wave coupling will mainly take place with negative harmonics $n \leq 0$. Moreover, the argument of the Bessel functions $\rho = -k_\perp v_\perp \gamma/\Omega_e$ is negative. Using the properties $J_{-n}(x) = (-1)^n J_n(x)$ and $J_n(-x) = (-1)^n J_n(x)$, the resonant diffusion can be specified for a beam interacting with electrons

$$D_{-n} = \pi \frac{e^2}{m_e^2} \lim_{V\to 0} \frac{1}{V} \int \frac{d^3k}{(2\pi)^4} |E_{\mathbf{k}}|^2 |\Theta_k^n|^2 \delta\left(\omega_b - k_\parallel v_\parallel - n\frac{\Omega_e}{\gamma}\right) \quad (13)$$

where $\rho_e = k_\perp v_\perp \gamma/\Omega_e$, $|E_{\mathbf{k}}|^2 = |E_{\mathbf{k},x}|^2 + |E_{\mathbf{k},y}|^2 + |E_{\mathbf{k},z}|^2$ and

$$\Theta_k^n = \frac{J_{n+1}(\rho_e)}{\sqrt{2}} \frac{E_{\mathbf{k},+}}{E_{\mathbf{k}}} + \frac{J_{n-1}(\rho_e)}{\sqrt{2}} \frac{E_{\mathbf{k},-}}{E_{\mathbf{k}}} + \frac{v_\parallel}{v_\perp} J_n(\rho_e) \frac{E_{\mathbf{k},\parallel}}{E_{\mathbf{k}}}. \quad (14)$$

Similar equations are the basis of EC wave interaction treatment in the bounce-average drift kinetic Fokker-Planck code LUKE [17]. In particular, it can be noted that Eq.13 is equivalent to equation 4.228 in LUKE's technical report [18].

3.2. Beam propagation and polarisation

In the next step, one should obtain the beam direction $(k_\parallel, k_\perp)$. Far from resonances, the propagation of an EC wave can be described in the cold plasma limit, which reads [1]

$$\left(\mathcal{S}\mathcal{N}^2 - \mathcal{R}\mathcal{L}\right)\left(\mathcal{N}^2 - \mathcal{P}\right)\tan^2\theta + \mathcal{P}\left(\mathcal{N}^2 - \mathcal{R}\right)\left(\mathcal{N}^2 - \mathcal{L}\right) = 0 \quad (15)$$

where $\mathcal{N} = c|\mathbf{k}|/\omega_b$ is the index of refraction, θ is the angle between the wave vector $\mathbf{k}$ and the magnetic field $\mathbf{B}_0$ ($\sin\theta = k_\perp/k$, $\cos\theta = k_\parallel/k$). In the dispersion relation, Eq.15, the Stix coefficients [19] are defined as

$$\mathcal{P} = 1 - \left(\frac{\omega_p}{\omega_b}\right)^2 \quad (16)$$

with $\omega_p = \sqrt{n_e e^2/(\epsilon_0 m_e)}$ the electron plasma frequency,

$$\mathcal{R} = \frac{\mathcal{P} - \frac{\Omega_e}{\omega_b}}{1 - \frac{\Omega_e}{\omega_b}}, \quad (17)$$

$$\mathcal{L} = \frac{\mathcal{P} + \frac{\Omega_e}{\omega_b}}{1 + \frac{\Omega_e}{\omega_b}}, \quad (18)$$

and $\mathcal{S} = (\mathcal{R} + \mathcal{L})/2$. The dispersion relation Eq.15 is a second order equation in $\mathcal{N}^2$ which possess two solutions. The first one, called the ordinary mode (O-mode),

corresponds to $\mathcal{N}^2 = \mathcal{P}$ for a perpendicular propagation $\left(\theta = \frac{\pi}{2}\right)$ and $\mathcal{N}^2 = \mathcal{L}$ for a parallel propagation ($\theta = 0$).

$$\mathcal{N}_O^2(\theta) = \frac{(\mathcal{RL} + \mathcal{SP})\tan^2\theta + \mathcal{P}(\mathcal{R} + \mathcal{L}) + \mathcal{G}_\theta}{2\left(\mathcal{S}\tan^2\theta + \mathcal{P}\right)} \tag{19}$$

where

$$\mathcal{G}_\theta = \sqrt{(\mathcal{SP} - \mathcal{RL})^2 \tan^4\theta + \mathcal{P}^2(\mathcal{L} - \mathcal{R})^2\left(\tan^2\theta + 1\right)}. \tag{20}$$

The second mode called the extraordinary mode (X-mode) corresponds to $\mathcal{SN}^2 = \mathcal{RL}$ for a perpendicular propagation and $\mathcal{N}^2 = \mathcal{R}$ for a parallel propagation.

$$\mathcal{N}_X^2(\theta) = \frac{(\mathcal{RL} + \mathcal{SP})\tan^2\theta + \mathcal{P}(\mathcal{R} + \mathcal{L}) - \mathcal{G}_\theta}{2\left(\mathcal{S}\tan^2\theta + \mathcal{P}\right)}. \tag{21}$$

An important property of the cold-plasma limit is the relative weight of the electric field components in the basis $(\mathbf{e}_x, \mathbf{e}_y, \mathbf{e}_z)$ defined in the first section. They read

$$i\frac{E_{\mathbf{k},y}}{E_{\mathbf{k},x}} = \frac{\mathcal{T}}{\mathcal{S} - \mathcal{N}^2} \tag{22}$$

where $\mathcal{T} = (\mathcal{R} - \mathcal{L})/2$ and

$$\frac{E_{\mathbf{k},z}}{E_{\mathbf{k},x}} = -\frac{\mathcal{N}^2\cos\theta\sin\theta}{\mathcal{P} - \mathcal{N}^2\sin^2\theta}. \tag{23}$$

For quasi-perpendicular propagation $\mathcal{N}_{X/O}(\theta)|\cos\theta| < v_T/c$, corresponding to the limit case implemented in the gyrokinetic code, thermal corrections to the cold-plasma dispersion relation are small except if $(\omega_p/\Omega_e)^2 \simeq (v_T/c)^2$ for the X-mode around the fundamental resonance, or if the assumption $(\omega_p/\Omega_e)^2 \ll 1$ breaks for the X-mode around the second harmonic resonance and for the O-mode around the fundamental resonance [20]. In the rest of this paper, we assume that the EC wave can be described in the cold plasma limit. The injection of Eq.22,23 in Eq.13,14 then leads to the approximated resonant diffusion coefficient

$$\tilde{D}_{-n} = \frac{\pi e^2 \mathcal{N}(\theta_0)}{m_e^2\omega_b}\frac{c}{|v_\parallel|}\lim_{V\to 0}\frac{1}{V}\int\frac{d^3k}{(2\pi)^4}|E_{\mathbf{k}}|^2\,\delta\left[\frac{\mathcal{N}(\theta)\cos(\theta) - \lambda\left(v_\parallel, v_\perp\right)}{\mathcal{N}(\theta_0)}\right]\left|\tilde{\Theta}_k^n\right|^2 \tag{24}$$

where

$$\lambda\left(v_\parallel, v_\perp\right) = \left(1 - \frac{\Omega_e}{\omega_b}\frac{n}{\gamma}\right)\frac{c}{v_\parallel} \tag{25}$$

and

$$\tilde{\Theta}_k^n = \frac{\begin{bmatrix}\left(1 + \frac{\mathcal{T}}{\mathcal{S}-\mathcal{N}^2(\theta)}\right)J_{n+1}(\tilde{\rho}_e) + \left(1 - \frac{\mathcal{T}}{\mathcal{S}-\mathcal{N}^2(\theta)}\right)J_{n-1}(\tilde{\rho}_e) \\ -2\frac{\mathcal{N}^2(\theta)\cos(\theta)\sin(\theta)}{\mathcal{P}-\mathcal{N}^2(\theta)\sin^2(\theta)}\frac{v_\parallel}{v_\perp}J_n(\tilde{\rho}_e)\end{bmatrix}}{2\sqrt{1 + \left(\frac{\mathcal{T}}{\mathcal{S}-\mathcal{N}^2(\theta)}\right)^2 + \left(\frac{\mathcal{N}^2(\theta)\cos\theta\sin\theta}{\mathcal{P}-\mathcal{N}^2(\theta)\sin^2\theta}\right)^2}} \tag{26}$$

with $\tilde{\rho}_e = \sin(\theta)\mathcal{N}(\theta)\frac{\omega_b}{\Omega_e}\frac{v_\perp}{c}\gamma$.

4. Broadening of the resonance by the finite width of the beam

4.1. Analytical treatment of the resonance

In practice, the beam possess a Gaussian shape of width W_0 in the direction perpendicular to its propagation. Due to the finite width of the beam, the Fourier transform of the electric field also possess a Gaussian shape of width $1/W_0$ in the direction perpendicular to $\mathbf{k}_0$. Moreover the amplitude of the wave-vector has to fulfill the dispersion relation. As a consequence the Fourier transform of the electric field takes the form

$$|E_{\mathbf{k}}|^2 = |E_{\mathbf{k},\mathbf{0}}|^2 \exp\left[-\left(\frac{\varphi}{\sigma}\right)^2\right] \exp\left[-\left(\frac{\theta-\theta_0}{\sigma}\right)^2\right] \delta\left(k - \frac{\mathcal{N}(\theta)\,\omega_b}{c}\right) k_0 \tag{27}$$

where θ_0 is the mean angle between the direction of propagation and the direction of the magnetic field and $\sigma = 1/(k_0 W_0)$, with $k_0 = \mathcal{N}(\theta_0)\,\omega_b/c$. Injecting this ansatz in Eq.24, one gets

$$\begin{aligned}\tilde{D}_{-n} = \frac{\pi e^2 \mathcal{N}(\theta_0)}{m_e^2 \omega_b} \frac{c}{|v_\parallel|} \lim_{V\to 0} \frac{1}{V} \frac{|E_{\mathbf{k},\mathbf{0}}|^2}{(2\pi)^4} k_0 k_{res}^2 \exp\left[-\left(\frac{\theta_{res}-\theta_0}{\sigma}\right)^2\right] \sin(\theta_{res}) \\ \times \left|\tilde{\Theta}^n_{k,res}\right|^2 \int_0^{2\pi} \exp\left[-\left(\frac{\varphi}{\sigma}\right)^2\right] d\varphi\end{aligned} \tag{28}$$

where $k_{res} = [\mathcal{N}(\theta_{res})\,\omega_b]/c$ and

$$\tilde{\Theta}^n_{k,res} = \frac{\left[\begin{array}{c}\left(1+\frac{\mathcal{T}}{\mathcal{S}-\mathcal{N}^2(\theta_{res})}\right) J_{n+1}(\tilde{\rho}_{res}) + \left(1-\frac{\mathcal{T}}{\mathcal{S}-\mathcal{N}^2(\theta_{res})}\right) J_{n-1}(\tilde{\rho}_{res}) \\ -2\frac{\mathcal{N}^2(\theta_{res})\cos(\theta_{res})\sin(\theta_{res})}{\mathcal{P}-\mathcal{N}^2(\theta_{res})\sin^2(\theta_{res})} \frac{v_\parallel}{v_\perp} J_n(\tilde{\rho}_{res})\end{array}\right]}{2\sqrt{1+\left(\frac{\mathcal{T}}{\mathcal{S}-\mathcal{N}^2(\theta_{res})}\right)^2 + \left(\frac{\mathcal{N}^2(\theta_{res})\cos\theta_{res}\sin\theta_{res}}{\mathcal{P}-\mathcal{N}^2(\theta_{res})\sin^2\theta_{res}}\right)^2}} \tag{29}$$

with $\tilde{\rho}_{res} = \sin(\theta_{res})\,\mathcal{N}(\theta_{res})\,\omega_b v_\perp \gamma/(\Omega_e c)$, and the resonant angle θ_{res} is solution of

$$\mathcal{N}(\theta_{res})\cos(\theta_{res}) = \lambda\left(v_\parallel, v_\perp\right). \tag{30}$$

For $v_\parallel = 0$, the resonance condition reads

$$\left(\frac{v_\perp}{c}\right)^2 = 1 - \left(\frac{\omega_b}{n\Omega_e}\right)^2 \tag{31}$$

which implies that there is a single point in the velocity space where resonance is possible. In practice, we will neglect the plasma-wave interaction for the case $v_\parallel = 0$.

The next step is to express the resonant diffusion coefficient as a function of the real electric field. To do so, we use Parseval's theorem

$$\begin{aligned}|E_{\mathbf{0}}|^2 &= \lim_{V\to 0} \frac{1}{V} \int \frac{d^3k}{(2\pi)^3} \int \frac{d\omega}{2\pi} |E_{\mathbf{k}}|^2 \\ &= \lim_{V\to 0} \frac{2|E_{\mathbf{k},\mathbf{0}}|^2 k_0 \omega^2}{V(2\pi)^4 c^2} \int_0^\pi \sin(\theta) \exp\left[-\left(\frac{\theta-\theta_0}{\sigma}\right)^2\right] \\ &\times \mathcal{N}^2(\theta)\, d\theta \int_0^{2\pi} d\varphi \exp\left[-\left(\frac{\varphi}{\sigma}\right)^2\right].\end{aligned} \tag{32}$$

Substituting this relationship in Eq.28, one gets

$$\tilde{D}_{-n} = \frac{\pi e^2 \mathcal{N}(\theta_0)}{2m_e^2\omega_b} \frac{c}{|v_\parallel|} |E_{\mathbf{0}}|^2 \frac{\sin(\theta_{res}) \exp\left[-\left(\frac{\theta_{res}-\theta_0}{\sigma}\right)^2\right] \mathcal{N}^2(\theta_{res})}{\int_0^\pi \sin(\theta) \exp\left[-\left(\frac{\theta-\theta_0}{\sigma}\right)^2\right] \mathcal{N}^2(\theta)\, d\theta} \left|\tilde{\Theta}^n_{k,res}\right|^2. \tag{33}$$

In practice, σ is often small compared to one. A good proxy of the resonant diffusion coefficient is therefore

$$\lim_{\sigma\to 0} \tilde{D}_{-n} = \frac{\sqrt{\pi} e^2 \mathcal{N}(\theta_0)}{2m_e^2\omega_b\sigma} \frac{c}{|v_\parallel|} |E_{\mathbf{0}}|^2 \exp\left[-\left(\frac{\theta_{res}-\theta_0}{\sigma}\right)^2\right] \left|\tilde{\Theta}^n_{k,res}\right|^2. \tag{34}$$

Even-tough this approximation is not used in the following of this paper, it could be used to lighten the numerical cost of the operator.

To construct the effective matrix of diffusion Eq.9, it is useful to express the vector $\mathbf{s}_n$, Eq.8, as function of θ

$$\begin{pmatrix} s_n^\perp \\ s_n^\parallel \end{pmatrix} = \begin{pmatrix} -\frac{n\Omega_e}{\omega_b\gamma} \\ \mathcal{N}(\theta_{res})\cos(\theta_{res})\,\frac{v_\perp}{c} \end{pmatrix} = \begin{pmatrix} -\frac{n\Omega_e}{\omega_b\gamma} \\ \lambda\left(v_\parallel, v_\perp\right)\frac{v_\perp}{c} \end{pmatrix}. \tag{35}$$

We deduce the values of $D_n^{\perp\perp}$, $D_n^{\perp\parallel}$ and $D_n^{\parallel\parallel}$ by multiplying Eq.33 by the appropriate combination of $s_n^\perp$ and $s_n^\parallel(\theta_{res})$.

4.2. Determination of θ_{res}

One of the difficulties left is the determination of θ_{res} which is solution of Eq.30. If $\lambda = 0$ then $\theta_{res} = \pi/2$. If $\lambda\left(v_\parallel, v_\perp\right) < 0$, we use the property

$$\mathcal{N}(\pi - \theta_{res})\cos(\pi - \theta_{res}) = -\lambda\left(v_\parallel, v_\perp\right) \tag{36}$$

to come back to a case where $\lambda > 0$. Using the dispersion relation (Eq.19 or 21) and the definitions of $\mathcal{R}$, $\mathcal{L}$ and $\mathcal{S}$, one gets after a bit of algebra

$$\begin{aligned} \mathcal{N}(\theta)\cos(\theta) &= \frac{1-\tau}{1+\tau} \\ &\times \frac{\left(\frac{\omega_b}{\Omega_e}\mathcal{P}(1+\tau)\right)^2 - 2\tau - \mathcal{P}\left(1+\tau^2\right) \pm (1-\mathcal{P})\sqrt{4\tau^2 + \left(\frac{\omega_b}{\Omega_e}\mathcal{P}(1-\tau^2)\right)^2}}{\left(\frac{\omega_b}{\Omega_e}\right)^2 \mathcal{P}(1+\tau)^2 - \mathcal{P}(1-\tau)^2 - 4\tau} \end{aligned} \tag{37}$$

where $\tau = \tan^2\left(\frac{\theta}{2}\right)$. At the resonance, $\omega_b \sim n\Omega_e$, and $\mathcal{N}(\theta)\cos(\theta)$ is therefore a function of t and $\mathcal{P}$ for a given harmonic n. The most commonly used modes of operation are O1, X2 and X3. For the O-mode, the cut-off implies $0 < \mathcal{P} < 1$, whereas for the X2 and X3 modes, the cut-off implies $1/n < \mathcal{P} < 1$ [1]. A numerical study represented in Fig.1 shows that $\mathcal{N}(\theta)\cos(\theta)$ is a strictly decreasing function of τ for the three modes of interest. It implies that Eq.30 possess a unique solution if and only if

$$\left|\lambda\left(v_\parallel, v_\perp\right)\right| \leq \mathcal{N}(\theta = 0). \tag{38}$$

This solution can be efficiently found by a binary search.

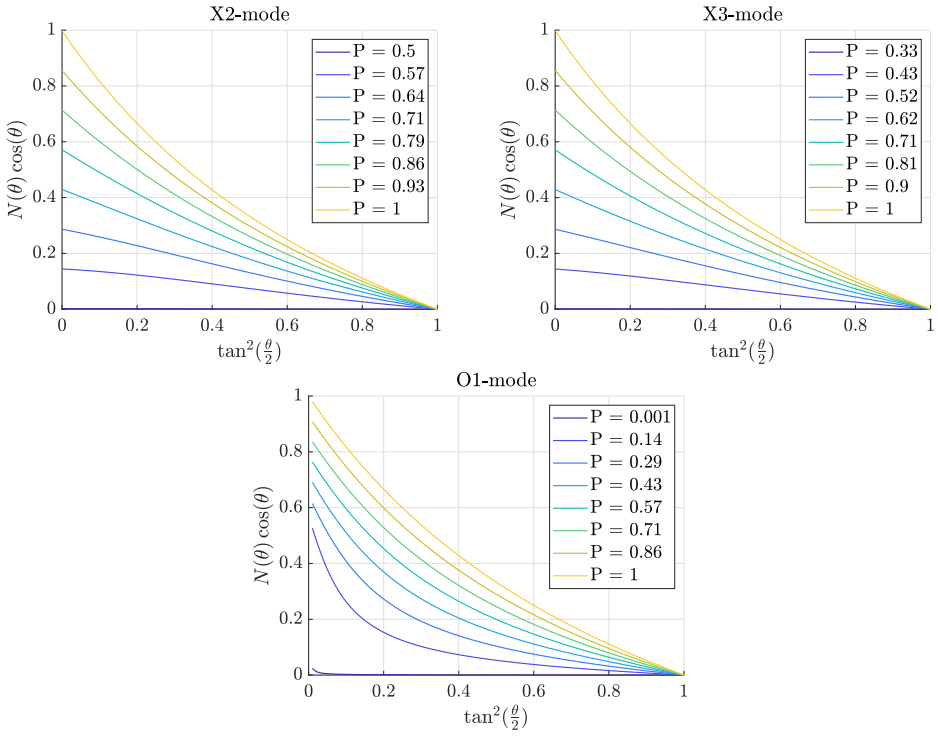

Figure 1. $\mathcal{N}(\theta)\cos(\theta)$ is a decreasing function of τ for the modes X2 (top left), X3 (top right) and O1 (bottom).

5. Specific case of a pure heating propagation along the mid-plane

5.1. Link between the amplitude of the electric field and the power carried by the beam

The theory developed in the previous sections is general, except for the use of the cold-plasma dispersion relation whose limits were already discussed. Spatial dependence of all quantities appearing in Eq.33 needs to be prescribed. For plasma quantities, spatial dependencies can directly be taken from the global gyrokinetic code. On the other hand, parameters related to the beam propagation should be computed with another code, e.g. a ray-tracing code. Moreover, an iterative interaction between the plasma and the beam codes is in principle required to accurately compute the power loss along the beam path due to plasma absorption. This is left for a future work. To avoid the coupling of the gyrokinetic code with a beam propagation code, a purely heating beam ($\theta_0 = \pi/2$) injected along the mid-plane is considered. Due to the axisymmetry, the beam propagates perpendicularly to the magnetic field ($\theta_0 = \pi/2$) everywhere. The beam width W_0 is assumed to be independent of the position for simplicity. The source is also assumed to be axisymmetric to increase the size of the interaction area in the 5D phase-space, easing the numerical handling of the resonance described in the next section.

The only free parameter left is the amplitude of electric field $|E_\mathbf{0}|^2$ as a function of space. Its value is related to the power of the beam. Indeed, the power of the beam

across a surface x reads

$$P = v_g \epsilon_0 \pi^{3/2} R W_0 \left|\mathbf{E}_{00}\right|^2 \tag{39}$$

where R is the major radius and $v_g = \left(\partial k/\partial \omega_b\right)^{-1}$ represents the group velocity at which the energy is supposed to flow and $|\mathbf{E}_{00}|$ represents the amplitude of the electric field at the center of the beam. The amplitude of the electric field is therefore given by

$$\left|\mathbf{E}_0\right|^2 (R,Z) = \frac{P\left(R\right)}{v_g\left(R\right)\epsilon_0 \pi^{3/2} R W_0} \exp\left[-\left(\frac{Z}{W_0}\right)^2\right] \tag{40}$$

where Z represents the vertical coordinate.

The group velocity can be computed for an exact perpendicular propagation $\theta_0 = \pi/2$. For the X-mode propagating perpendicularly to the magnetic field, the group velocity reads

$$\begin{aligned} v_g^X &= \mathcal{N}_X\left(\frac{\pi}{2}\right) c \frac{\left[\omega_b^2 - \left(\omega_p^2 + \Omega_e^2\right)\right]^2}{\left[\omega_b^2 - \left(\omega_p^2 + \Omega_e^2\right)\right]^2 + \omega_p^2 \Omega_e^2} \\ &= \mathcal{N}_X\left(\frac{\pi}{2}\right) c \frac{\mathcal{S}^2\left[1 - \left(\frac{\Omega_e}{\omega_b}\right)^2\right]}{\mathcal{S}^2\left[1 - \left(\frac{\Omega_e}{\omega_b}\right)^2\right] - \frac{\Omega_e}{\omega_b}\mathcal{T}}. \end{aligned} \tag{41}$$

For the O-mode propagating perpendicularly to the magnetic field, the group velocity reads

$$v_g^O = \mathcal{N}_O\left(\frac{\pi}{2}\right) c. \tag{42}$$

5.2. Model for the evolution of the beam power along the path

To determine the evolution of the beam power along its path, a simple model of absorption derived by Bornatici [21] is used. The local absorption coefficient of a X-polarized wave propagating quasi-perpendicularly to the background magnetic field ($\mathcal{N}_X|\cos(\theta)| < v_T/c$), where $v_T = \sqrt{T_e/m_e}$ is the thermal velocity of electrons, of a weakly relativistic ($v_T/c \ll 1$) cold Maxwellian plasma, assuming that Finite Larmor Radius effects can be neglected ($\omega_p^2 < \Omega_e^2$), reads [22]

$$\alpha_n^{(X)}(\theta) = \alpha_n(\theta)\ \phi_{n+\frac{3}{2}}(\omega_b)\ \mu_n^{(X)}(\theta) \tag{43}$$

for $n \geq 2$, where n is the harmonic number and

$$\alpha_n(\theta) = \frac{\pi n^{2n-1}}{2^n \Gamma\left(n\right)} \left(\frac{v_T}{c}\right)^{2(n-1)} \frac{\omega_p^2}{c} \left(1 + \cos^2\theta\right) \left(\sin\theta\right)^{2(n-1)} \tag{44}$$

where Γ is the Euler integral of the second kind and the relativistic profile of the resonance is given by

$$\phi_q(\omega_b) = \begin{cases} \frac{1}{\Gamma(q)} \left(\frac{c}{v_T}\right)^{2q} \left(\frac{n\Omega_e - \omega_b}{\omega_b}\right)^{q-1} \frac{1}{\omega_b} \exp\left[-\frac{c^2}{v_T^2} \frac{n\Omega_e - \omega_b}{\omega_b}\right] & \text{if } \ \omega_b < n\Omega_e \\ 0 & \text{otherwise} \end{cases} \tag{45}$$

and

$$\mu_n^{(X)}(\theta) = \left[\mathcal{N}_X\left(\theta\right)\right]^{2n-3} \left[1 + \frac{(\omega_p/\Omega_e)^2}{n\left(n^2 - 1 - (\omega_p/\Omega_e)^2\right)}\right]^2 \quad \text{for } n \geq 2 \tag{46}$$

Given the finite width in θ, the local absorption coefficient should be integrated over angles

$$\begin{aligned}\tilde{\alpha} &= \int_0^{\pi} \alpha_n^{(X)}(\theta)\mathcal{F}(\theta)\,d\theta \\ &= \int_{-\theta_0}^{\pi-\theta_0} \alpha_n^{(X)}(\theta_0+\Delta\theta)\exp\left[-\frac{\Delta\theta^2}{2\sigma^2}\right]\frac{d(\Delta\theta)}{\sigma\sqrt{2\pi}} \\ &= \int_{-\theta_0}^{\pi-\theta_0} \left[\alpha_n^{(X)}(\theta_0)+\Delta\theta\frac{\alpha_n^{(X)}}{d\theta}(\theta_0)+\mathcal{O}\left(\Delta\theta^2\right)\right]\exp\left[-\frac{\Delta\theta^2}{2\sigma^2}\right]\frac{d(\Delta\theta)}{\sigma\sqrt{2\pi}} \\ &= \alpha_n^{(X)}(\theta_0)+\mathcal{O}\left[\left(\frac{\sigma}{\theta_0}\right)^2\right] \end{aligned} \tag{47}$$

where the first order correction term has been neglected by using its parity in combination with the hypothesis $\sigma \ll \theta_0$. As a consequence of Eq.47, only the leading order term is kept, implying that Eq.43 is in practice evaluated in θ_0.

The optical thickness of the plasma τ_X is defined by the integral of the absorption coefficient along the beam path $\tau_X = \int_0^L \alpha_n^{(X)}(\theta_0)\mathrm{d}s$, with s the curvilinear abscissa along the beam path of length L. The beam power is then given by $P_{EC} = P_{EC,0}\exp(-\tau_X)$. The same methodology applies to the O-mode, considering for $n \geq 1$

$$\alpha_n^{(O)}(\theta) = \alpha_n(\theta)\ \phi_{n+\frac{5}{2}}(\omega_b)\ \left[\mathcal{N}_O(\theta)\right]^{2n-1}\left(\frac{v_T}{c}\right)^2 \tag{48}$$

The simple absorption model of Bornatici has been compared against the linear Landau damping calculation of the C3PO Ray Tracing code [23], using a range of TCV-like plasma equilibria. An analytic MHD equilibria has been used, based on Grad-Shafranov solution and assuming Solov'ev profiles, derived by Cerfon and Freidberg [24]. It assumes that the pressure profile evolves as $1-\rho^2$, where ρ is the square root of normalized poloidal magnetic flux, and the density profiles is proportional to $\sqrt{1-\rho^2}$. The temperature profile is deduced from pressure and density profiles, using $n_{e,edge} = n_{e,0}/20$ and $T_{e,edge} = T_{e,0}/20$. The on-axis magnetic field has been fixed to $B_0 = 1.5$ T and a pure-ECRH X2 beam at 75 GHz is launched from the outer midplane.

Figure 2 shows a poloidal view of C3PO simulation results and an example of the EC beam power along a ray path obtained both with C3PO and Bornatici's analytic model. The absorption occurs at the same location in both cases, while the absorption level is slightly lower with the analytic model. Temperature and density scans are shown in figure 3 and 4 respectively. The absorption level and the absorption characteristic length (taken between $P_{abs}/P_{abs,max} = 0.9$ and $P_{abs}/P_{abs,max} = 0.1$) are compared. In general, Bornatici's model absorbs slightly less power, over a slightly longer length than C3PO simulations. This effect tends to reduce for better absorption conditions (higher density and temperature) and the overall agreement between both method is rather good within TCV parameters range.

6. Numerical handling of the source term

In the previous section, an ECRH source has been derived with the aim of an easy implementation in a flux-driven gyrokinetic code. There are different numerical approaches to implement the gyrokinetic equations: Eulerian, Lagrangian, semi-Lagrangian [25]. Up to now, the choice of the gyrokinetic code was unspecified. We

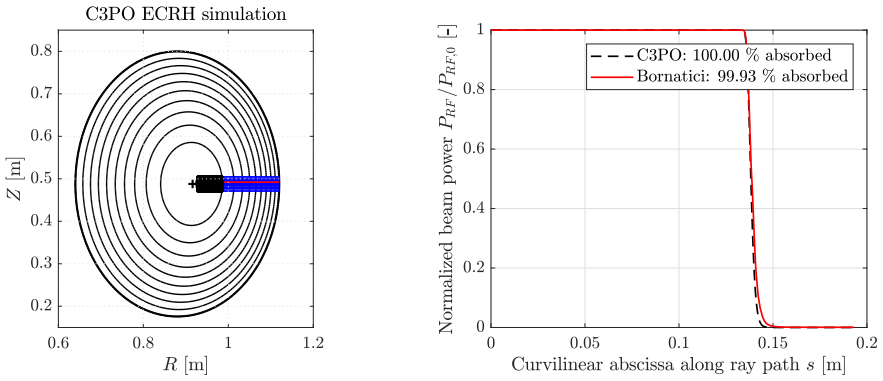

Figure 2. Left: poloidal view of a pure-ECRH C3PO simulation in a TCV-like plasma ($n_{e,0} = 2 \cdot 10^{19}$ m^{-3}, $T_{e,0} = 2 \cdot 10^3$ eV and $B_0 = 1.5$ T), for a X2 EC beam at 75 GHz. Black dots represent the maximum of absorption. Right: Power profile along the red ray of the left plot, computed with C3PO and with Bornatici's analytic model.

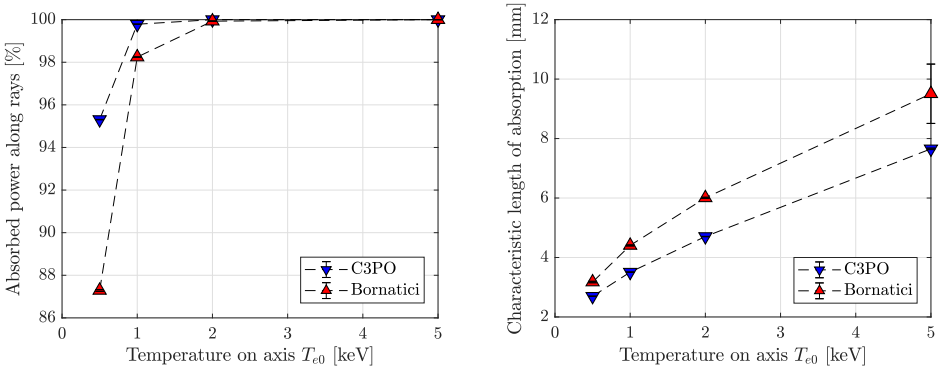

Figure 3. Temperature scan comparing Bornatici's analytic model and C3PO pure-ECRH simulations for $n_{e,0} = 2 \cdot 10^{19}$ m^{-3}, $T_{e,0} = 0.5\text{-}5 \cdot 10^3$ eV, $B_0 = 1.5$ T and a X2 EC beam at 75 GHz. Left: absorption level. Right: absorption characteristic length.

now make the choice to use the ORB5 code [13] which is using a particle-in-cell (PIC) approach.

6.1. Fokker-Planck form

As suggested in [26], quasi-linear wave-particle interaction can be efficiently implemented in PIC codes using a Langevin approach. To do so, the first step consists in expressing Q_n in the form of a Fokker-Planck operator

$$Q_n = \nabla_{\mathbf{v}} \cdot [\nabla_{\mathbf{v}} \cdot (\mathbb{D}_n F) - \mathbf{\Gamma}_n F] \tag{49}$$

where the drag force is defined as

$$\mathbf{\Gamma}_n = \nabla_{\mathbf{v}} \cdot \mathbb{D}_n \tag{50}$$

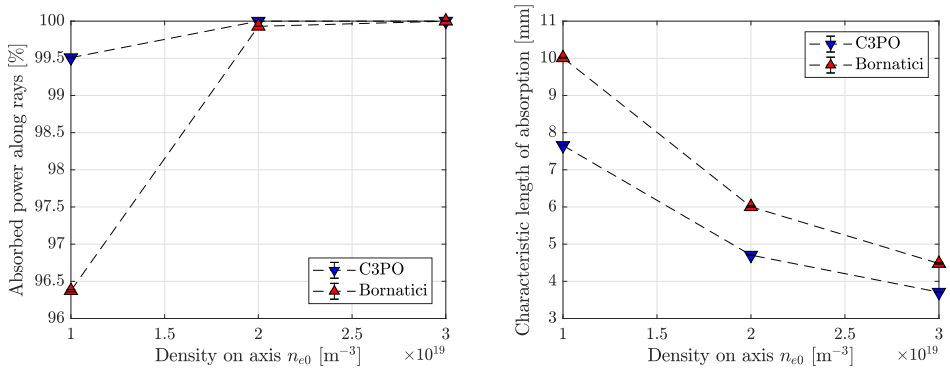

Figure 4. Density scan comparing Bornatici's analytic model and C3PO pure-ECRH simulations for $n_{e,0} = 0.5\text{-}3 \cdot 10^{19}$ m^{-3}, $T_{e,0} = 2 \cdot 10^3$ keV, $B_0 = 1.5$ T and a X2 EC beam at 75 GHz. Left: absorption level. Right: absorption characteristic length.

The divergence of a second-order tensor field in cylindrical polar coordinates where there is no φ dependence is given by

$$\mathbf{\Gamma}_n = \nabla_{\mathbf{v}} \cdot \mathbb{D}_n = \Gamma_n^{\perp} \hat{\mathbf{e}}_{\perp} + \Gamma_n^{\parallel} \hat{\mathbf{e}}_{\parallel} \tag{51}$$

with

$$\Gamma_n^{\perp} = \frac{1}{v_{\perp}} \frac{\partial \left(v_{\perp} D_n^{\perp\perp} \right)}{\partial v_{\perp}} + \frac{\partial D_n^{\perp\parallel}}{\partial v_{\parallel}} \tag{52}$$

$$\Gamma_n^{\parallel} = \frac{1}{v_{\perp}} \frac{\partial \left(v_{\perp} D_n^{\perp\parallel} \right)}{\partial v_{\perp}} + \frac{\partial D_n^{\parallel\parallel}}{\partial v_{\parallel}} \tag{53}$$

In most of the velocity space, centered finite differences are used to numerically estimate the drag terms. An exception is made for markers with low parallel velocities. Indeed the term $c/\left|v_{\parallel}\right|$ in Eq.33 implies a quick variation of the resonant diffusion coefficient for low parallel velocities. These variations are difficult to treat numerically. An approximate version of the drag terms is used for markers with a parallel velocity lower than a given value ($\left|v_{\parallel}\right| \leq v_{lim}$). In practice, the value $v_{lim} = 0.1 v_T$ is chosen. To compute the approximate drag terms, we use the fact that $s_{\parallel} \ll s_{\perp}$, even for low parallel velocities compared to the thermal velocity, to discard terms proportional to $D_n^{\perp\parallel}$ and $D_n^{\parallel\parallel}$. The parallel drag is therefore approximated to be zero. Moreover the main dependence of the resonant diffusion coefficient with respect to $v_{\perp}$ is in the Bessel function for the X-mode. A good proxy for Eq.52 in the case of a X-mode is therefore given by

$$\Gamma_{n,\left|v_{\parallel}\right| \leq v_{lim}}^{\perp} = D_n^{\perp\perp} \left[\frac{1}{v_{\perp}} + \frac{J_{n-2}\left(\tilde{\rho}_{res}\right)}{J_{n-1}\left(\tilde{\rho}_{res}\right)} \frac{\partial \tilde{\rho}_{res}}{\partial v_{\perp}} \right]. \tag{54}$$

It is possible to use the fact that $\tilde{\rho}_{res} \ll 1$ to further approximate Eq.54. Indeed the Bessel functions are well approximated by $J_n(x) \simeq (x/2)^n / n!$ for $x \ll 1$. Using these properties, the drag terms are well approximated by

$$\Gamma_{n,\left|v_{\parallel}\right| \leq v_{lim}}^{\perp} = \frac{D_n^{\perp\perp}}{v_{\perp}} (2n - 1) \tag{55}$$

$$\Gamma^{\parallel}_{n,|v_\parallel|\leq v_{lim}} = 0. \tag{56}$$

A similar calculation can be performed for the O-mode and leads to the same approximate result for the drag term. Therefore Eq.55 and 56 are used for both modes for markers with low parallel velocities ($|v_\parallel| \leq v_{lim}$).

6.2. Langevin form

In order to efficiently solve the Fokker-Planck equation, we shall find and solve the underlying stochastic process. Such a process can be found by deploying Ito's lemma for Fokker-Planck type equation as used for the collision operator in ORB5 [27]. Hence, solution to Eq.49 is equivalent to the solution of the stochastic process

$$d\mathbf{v} = \sum_n \left(\mathbf{\Gamma}_n dt + \mathbb{G}_n d\mathbf{W}\right) \tag{57}$$

where $d\mathbf{W} = \mathbf{W}_{t+dt} - \mathbf{W}_t$ is a Wiener process with increments which follows Gaussian distribution, and $\mathbb{G}_n \cdot \mathbb{G}_n^T = 2\mathbb{D}_n$. Eq.57 is discretised using the Euler-Maruyama scheme. The evolution of the marker position in the velocity space then reads

$$\Delta\mathbf{v}_i = \sum_n \left(\mathbf{\Gamma}_{n,i}\Delta t + \mathbb{G}_{n,i}\sqrt{\Delta t}\mathbf{R}_i\right) \tag{58}$$

where i is the index of the marker considered, $\mathbf{\Gamma}_{n,i}$ and $\mathbb{G}_{n,i}$ are evaluated at the position in the 5d phase space of the marker before the kick and

$$\mathbf{R}_i = \begin{pmatrix} R_i^{\perp} \\ R_i^{\parallel} \end{pmatrix} \tag{59}$$

where $R_i^{\perp}$, $R_i^{\parallel}$ are independent random numbers sampled from Gaussian distributions with zero mean and a variance of one. Any $\mathbb{G}_{n,i}$ such as $\mathbb{G}_{n,i} \cdot \mathbb{G}_{n,i}^T = 2\mathbb{D}_{n,i}$ gives exactly the same dynamics. One solution is given by

$$\mathbb{G}_{n,i} = \sqrt{2D_{n,i}} \begin{pmatrix} 0 & s_{n,i}^{\perp} \\ 0 & s_{n,i}^{\parallel} \end{pmatrix} \tag{60}$$

In summary, Eq.57 is in the specific case considered here

$$\begin{pmatrix} \Delta v_{\perp,i} \\ \Delta v_{\parallel,i} \end{pmatrix} = \sum_n \left[\begin{pmatrix} \Gamma_{n,i}^{\perp} \\ \Gamma_{n,i}^{\parallel} \end{pmatrix} \Delta t + \sqrt{2D_{n,i}\Delta t} \begin{pmatrix} s_{n,i}^{\perp} \\ s_{n,i}^{\parallel} \end{pmatrix} R_i^{\parallel} \right] \tag{61}$$

Note that the contribution of $R_i^{\perp}$ completely disappeared. This is due to the special form of $\mathbb{D}_n$ which possess one zero eigenvalue. In other words, the diffusion is unidirectional along the vector $\mathbf{s}_n$.

7. Numerical tests of the source term implemented in ORB5

The source operator described in the previous sections has been implemented in the global gyrokinetic code ORB5 [13]. In this section, the implementation is verified by studying the evolution of the distribution function due to this source term. All other modules of the code (movement of markers, collisions...) are turned-off for simplicity. As a consequence, the distribution function evolves only due to the source, according to Eq.2.

7.1. Description of the test

In the tests performed in this section, flat profiles of density n_e and temperature T_e are used. The density and temperature are scanned around reference values $n_{e,ref} = 1 \cdot 10^{19}$ m^{-3} for density, $T_{e,ref} = 1.2 \cdot 10^3$ eV for the temperature. An analytical axisymmetric magnetic geometry with circular concentric flux surfaces has been used for these tests [28]. The magnetic field reads $\mathbf{B} = \frac{B_0 R_0}{R}\left[\frac{\epsilon}{\bar{q}}\mathbf{e}_\chi + \mathbf{e}_\Phi\right]$ where χ stands for the poloidal angle, Φ for the toroidal angle, $\epsilon = \frac{r}{R_0}$ is the inverse aspect ratio and $\bar{q}(r) = q(r)\sqrt{1-\epsilon^2}$ with q the safety factor. The on-axis magnetic field intensity has been fixed to $B_0 = 1.4$ T and a constant value for $\bar{q} = 10$ has been used. With this choice the poloidal component of the magnetic field is negligible. The minor and major radii have been fixed respectively to $a = 25$ cm, $R_0 = 88$ cm which are values typical of TCV. The frequency and the width of the beam have been scanned around reference values, $f_{ref} = 78$ GHz and $W_{0,ref} = 2$ cm respectively. Most of the results presented here are done with a X2 heating. The results obtain with a O2 heating is presented only for the reference parameters.

The numerical tests shown in this section have been performed with $4 \cdot 10^7$ of markers on a simulation domain with a minor radius ranging from $r_{min} = 0$ to $r_{max} = 0.2a$. This is a regular density of markers for ORB5. Results are converged with respect to the number of markers. The time step is chosen to ensure the condition $\max_{\mathbf{r},\mathbf{v}}(D_n)\Delta t \ll 1$. For realistic values of the beam intensity ($\sim 10^5$ W), this condition is satisfied with time steps typically chosen for simulations in presence of electrons. In practice for the tests presented here the time step has been fixed to $\Delta t = 1\Omega_i^{-1}$ where $\Omega_i = eB/m_i$ is the cyclotron frequency of a proton. The beam power at the entry of the plasma has been fixed to $P_0 = 1$ W to ensure that the condition $\max_{\mathbf{r},\mathbf{v}}(D_n)\Delta t \ll 1$ is fulfilled. The linear dependency of the source with the beam power allows to extrapolate the results obtain here to an arbitrary power input at the condition to have a time step small enough.

7.2. Velocity dependence of the resonant diffusion coefficient

The resonant diffusion coefficient Eq.33 possess dependencies in the poloidal plane and in the velocity space. In Fig.5, the velocity dependence of the resonant diffusion coefficient of the reference case is represented at mid-plane and for the radial position where the absorption is maximal. The red circle in Fig.5 corresponds to the solution of the resonant condition for the dominant angle θ_0, which reads for the special case of a pure perpendicular propagation $(v/c)^2 = 1 - [\omega_b/(n\Omega_e)]^2$. The maximum of the diffusion coefficient is slightly above the red circle in the direction of increasing $v_\perp$ because of the dependency of the argument of the Bessel functions $\tilde{\rho}_{res}$ in Eq.29, with respect to this variable. The factor $c/|v_\parallel|$ in Eq.33 implies that the maximum of the resonant diffusion coefficient of the X-mode is reached for low but non zero parallel velocities. As a consequence, velocity derivatives of the resonant diffusion coefficient close to the zero parallel velocity axis are difficult to handle numerically. The drag terms are therefore computed approximately in this region as described in the section 6.1.

In Fig.6, the resonant diffusion coefficient is plotted for a O2 beam. All other parameters are the same as for the reference case. A major difference with the reference X2 mode is the amplitude of the diffusion coefficient which is much lower compared with the one of the X2 mode. This is a due to the fact that for the O2 mode, the

electric field is mainly aligned with the magnetic field. On the other hand for the X2 mode the electric field is mainly perpendicular to the magnetic field. Given the different orders of the Bessel functions in front of the components of the electric field in Eq.14 a better coupling of the X-mode is expected compared with the O-mode. The qualitative difference in the shape of the diffusion coefficient between the O2 and the X2 modes is also a consequence of the difference of polarisation between the modes. Indeed, in Eq.14, the is a factor $\frac{v_\parallel}{v_\perp}$ in front of the term proportional to the parallel component of the electric field. This factor implies that the maximum of the resonant diffusion coefficient of the O-mode corresponds to higher parallel velocity compared with the one of the X-mode. Therefore there is less difficulty to treat drag terms for low parallel velocity markers in the case of a O-mode beam compared with the X-mode case. The approximation of the drag terms described in the section 6.1 is nevertheless applied for better results and consistency with the X-mode.

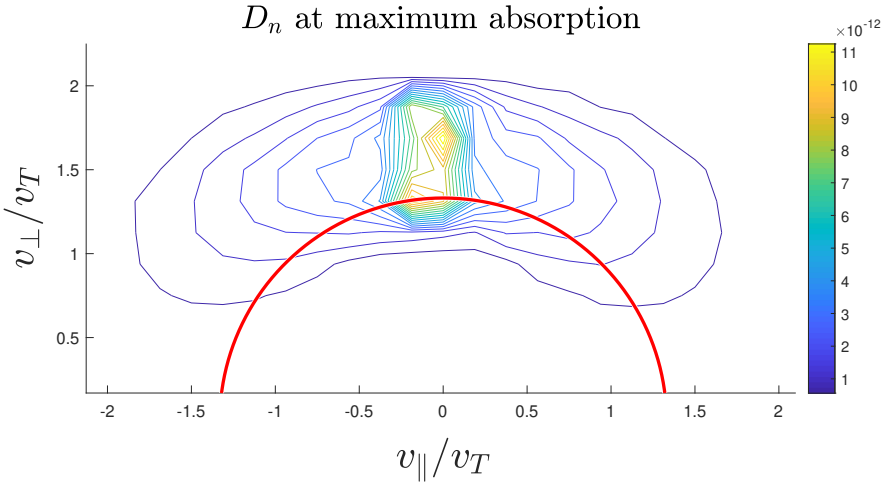

Figure 5. Effective diffusion coefficient at the maximum of absorption for the reference case (X2, $f = 78$ GHz, $W_0 = 2$ cm, $n_e = 10^{19}$ m^{-3}, $T_e = 1.2 \cdot 10^3$ eV). The diffusion coefficient is given in units $v_T^2 \Omega_e$.

7.3. Absorption profiles

The power deposited on electrons can be computed by using the evolution of the marker position in velocity space. Indeed, for one given marker i, the energy evolution due to one kick can be computed with the use of Eq.61 and reads

$$\Delta\left(v_i^2\right) = 2\left(v_{\parallel,i}\Delta v_{\parallel,i} + v_{\perp,i}\Delta v_{\perp,i}\right) + \left(\Delta v_{\parallel,i}\right)^2 + \left(\Delta v_{\perp,i}\right)^2 \tag{62}$$

Eq.62 can be ensemble average and divided by the time step. This leads to

$$\frac{\left\langle\Delta\left(v_i^2\right)\right\rangle}{\Delta t} = 2\sum_n \left[v_{\parallel,i}\Gamma^{\parallel}_{n,i} + v_{\perp,i}\Gamma^{\perp}_{n,i} + D_{n,i}\left[\left(s^{\parallel}_{n,i}\right)^2 + \left(s^{\perp}_{n,i}\right)^2\right]\right] + \Delta t\sum_n \left[\left(\Gamma^{\parallel}_{n,i}\right)^2 + \left(\Gamma^{\perp}_{n,i}\right)^2\right] \tag{63}$$

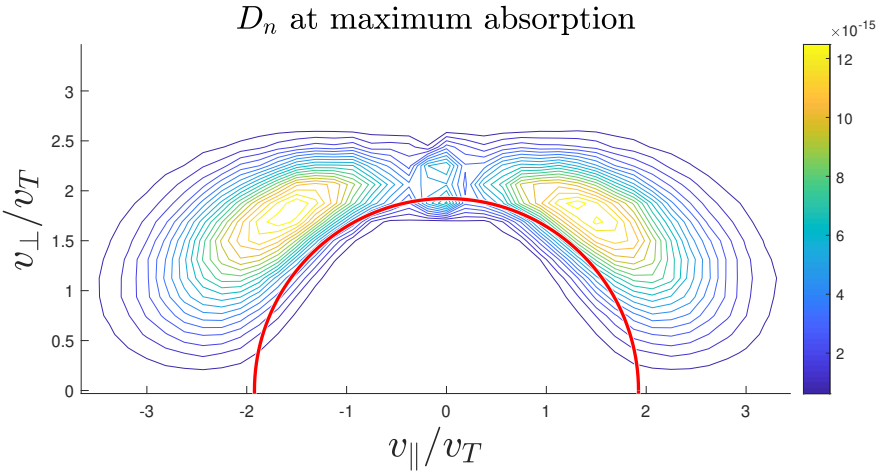

Figure 6. Effective diffusion coefficient at the maximum of absorption for the O2 mode. All other parameters are the same as for the reference case ($f = 78$ GHz, $W_0 = 2$ cm, $n_e = 10^{19}$ m^{-3}, $T_e = 1.2 \cdot 10^3$ eV). The diffusion coefficient is given in units $v_T^2 \Omega_e$.

By multiplying this quantity by the weight of the marker times $\frac{m_e}{2}$, and by summing over the markers in a spatial bin, one gets access to the ensemble average power deposition on this bin. Note that Eq.63 allows to put a quantitative limit for the maximum time step which is allowed for a given source amplitude.

In Fig.7, the ensemble average power deposited by the ORB5 source is plotted as a function of the major radius and compared with Bornatici's absorption model for the reference case. A good agreement is found for the amplitude, the width and the position of absorption. The small discrepancy between ORB5 results and the prediction of Bornatici for the total power absorbed is the consequence of the approximate drag terms used for low parallel velocities and described in the section 6.1. The two dotted lines in Fig.7 corresponds respectively to the major radii where $\omega_b = n\Omega_e$ and $\omega_b = n\Omega_e\sqrt{1-(3v_T/c)^2}$. Most of the deposition power deposition is expected in between these two positions which then gives a good proxy for the width of the deposition area.

In Fig.8 the ensemble average power deposited by the ORB5 source is plotted as a function of the major radius for the O2-mode with the same parameters as the reference case. The fraction of power deposited is as expected much lower than the one of the X2-mode. In the figures 9, 10 and 11, scans in density, temperature and the beam frequency are respectively represented. For all these parameters a good agreement for the position, the amplitude and the width of the power deposition is found. A scan with respect with the beam width W_0 has also been performed and is not represented here. As expected from Bornatici's prediction, this parameters has a negligible impact on the radial profile of absorption.

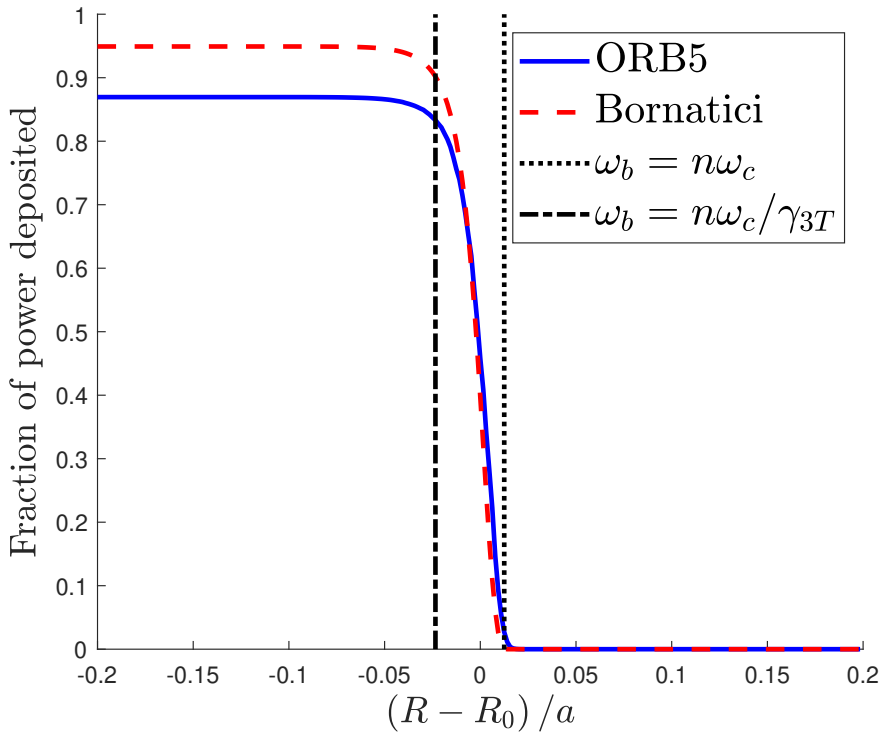

Figure 7. Fraction of the power deposited as a function of the major radius for the reference case (X2, $f = 78$ GHz, $W_0 = 2$ cm, $n_e = 10^{19}$ m^{-3}, $T_e = 1.2 \cdot 10^3$ eV).

Conclusion

In this paper, a quasilinear operator describing the interaction of a beam with electrons in a magnetised plasma is derived. This operator is well suited for an efficient numerical implementation thanks to an analytical treatment of the resonance, relying on the finite width of the plasma beam.

A specific case, corresponding to a perpendicular injection on the midplane has been implemented in the gyrokinetic code ORB5 using the equivalence between Fokker-Planck and Langevin equations. This specific case, corresponding to a pure heating scheme, allows to treat the propagation of the beam without the usage of a beam propagation code. To avoid a costly iteration between the beam intensity and the power absorbed by the plasma, the beam amplitude is computed thanks to an analytical model.

The numerical source implementation has been verified by studying the shape of the source term both in velocity and real space and by performing scans in different physical quantities known to modify the power deposition. A good agreement is found between the numerical results and the theoretical expectation.

In a forthcoming article, the effects of the source term presented in this article on the transport will be studied in details. The more general case of a non-perpendicular beam injection also be implemented and studied.

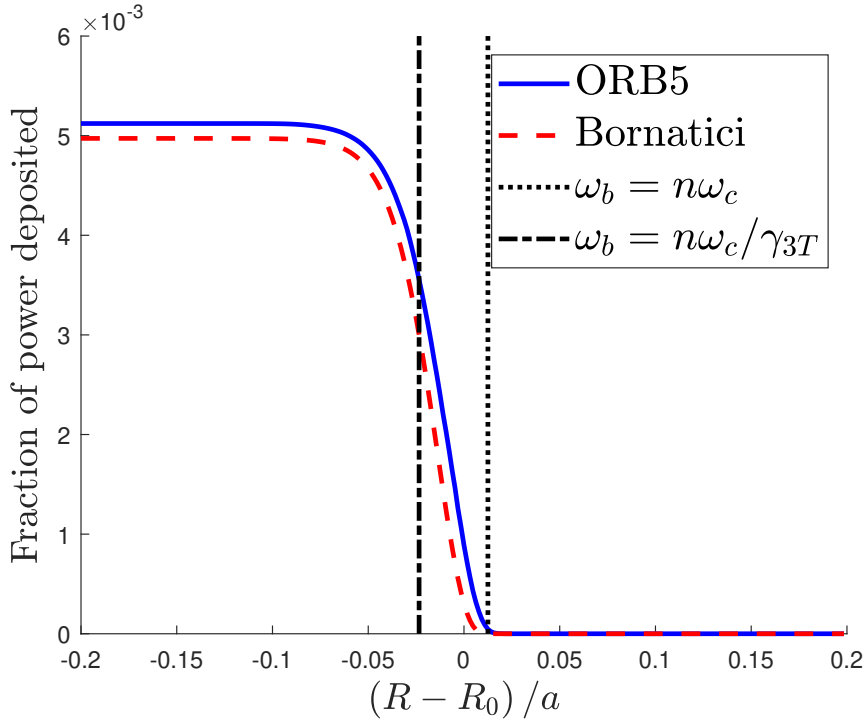

Figure 8. Fraction of the power deposited as a function of the major radius for the O2-mode. All other parameters are the same as for the reference case ($f = 78$ GHz, $W_0 = 2$ cm, $n_e = 10^{19}$ m^{-3}, $T_e = 1.2 \cdot 10^3$ eV).

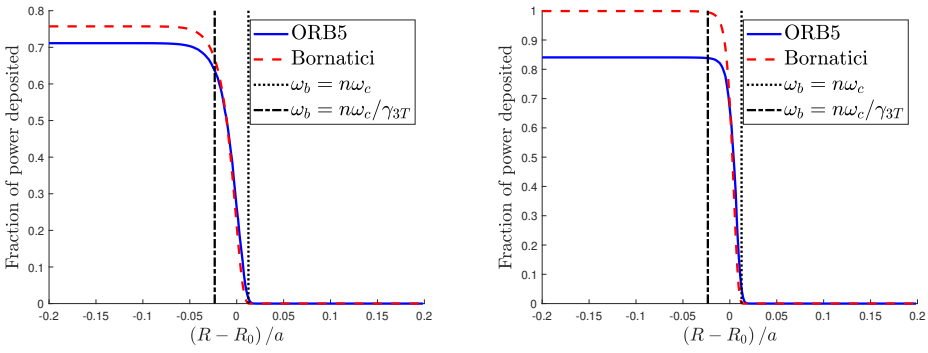

Figure 9. Fraction of the power deposited as a function of the major radius for different densities. On the left plot, the density is $n_e = 5 \cdot 10^{18}$ m^{-3}, whereas on the right plot it is $n_e = 2 \cdot 10^{19}$ m^{-3}. The other parameters are unchanged compared with the reference case (X2-mode, $f = 78$ GHz, $W_0 = 2$ cm, $T_e = 1.2 \cdot 10^3$ eV).

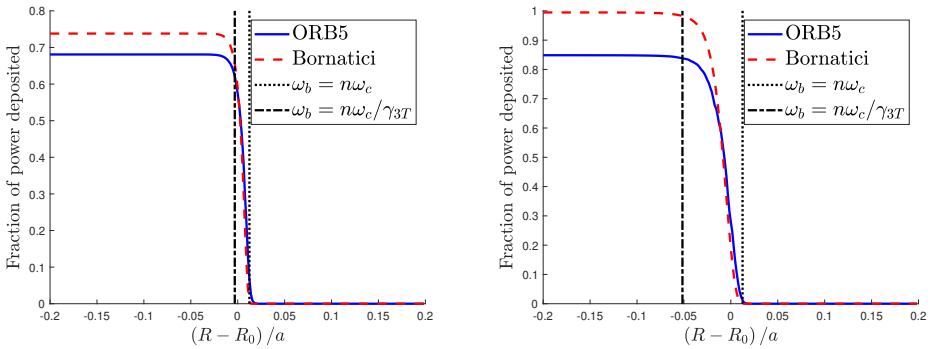

Figure 10. Fraction of the power deposited as a function of the major radius for different temperatures. On the left plot, the temperature is $T_e = 5.4 \cdot 10^2$ eV, whereas on the right plot it is $T_e = 2.2 \cdot 10^3$ eV. The other parameters are unchanged compared with the reference case (X2-mode, $f = 78$ GHz, $W_0 = 2$ cm, $n_e = 10^{19}$ m^{-3}).

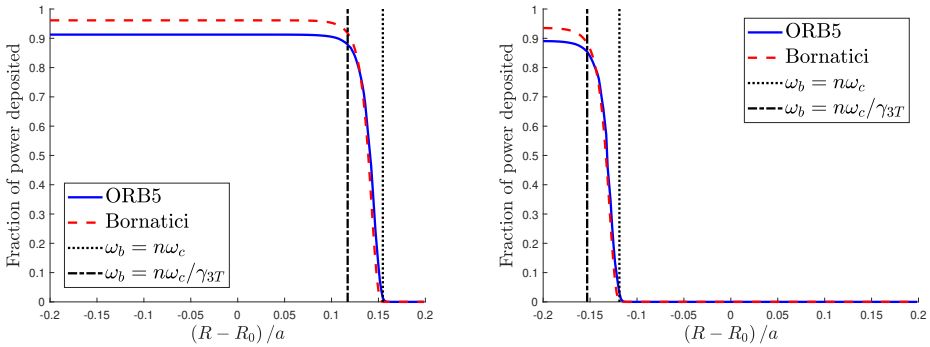

Figure 11. Fraction of the power deposited as a function of the major radius for different frequencies. On the left plot, the frequency of the beam is $f_{beam} = 75$ GHz, whereas on the right plot it is $f_{beam} = 81$ GHz. The other parameters are unchanged compared with the reference case (X2-mode, $W_0 = 2$ cm, $n_e = 10^{19}$ m^{-3}, $T_e = 1.2 \cdot 10^3$ eV).

Acknowledgement

This work was supported by a grant from the Swiss National Supercomputing Centre (CSCS) under project s909. This work has been carried out within the framework of the EUROfusion Consortium and has received funding from the Euratom research and training programme 2014-2018 and 2019-2020 under grant agreement No 633053. The views and opinions expressed herein do not necessarily reflect those of the European Commission.

References

[1] R. Prater. Heating and current drive by electron cyclotron waves. *Physics of Plasmas*, 11(5):2349–2376, 2004.

[2] S. Coda, S. Alberti, P. Blanchard, T. P. Goodman, M. A. Henderson, P. Nikkola, Y. Peysson,

and O. Sauter. Electron cyclotron current drive and suprathermal electron dynamics in the TCV tokamak. *Nuclear Fusion*, 43(11):1361–1370, 2003.

[3] Y. Peysson, J. Decker, L. Morini, and S. Coda. RF current drive and plasma fluctuations. *Plasma Physics and Controlled Fusion*, 53(12):124028, 2011.

[4] O. Chellaï, S. Alberti, M. Baquero-Ruiz, I. Furno, T. Goodman, F. Manke, G. Plyushchev, L. Guidi, A. Köhn, O. Maj, E. Poli, K. Hizanidis, L. Figini, and D. Ricci. Millimeter-wave beam scattering by field-aligned blobs in simple magnetized toroidal plasmas. *Phys. Rev. Lett.*, 120:105001, 2018.

[5] O. Chellaï, S. Alberti, M. Baquero-Ruiz, I. Furno, T. Goodman, B. Labit, O. Maj, P. Ricci, F. Riva, L. Guidi, and E. Poli. Millimeter-wave beam scattering by edge-plasma density fluctuations in TCV. *Plasma Physics and Controlled Fusion*, 61(1):014001, 2018.

[6] A. Snicker, E. Poli, O. Maj, L. Guidi, A. Köhn, H. Weber, G. Conway, M. Henderson, and G. Saibene. The effect of density fluctuations on electron cyclotron beam broadening and implications for ITER. *Nuclear Fusion*, 58(1):016002, 2017.

[7] R.W. Harvey, O. Sauter, R. Prater, and P. Nikkola. Radial transport and Electron-Cyclotron-Current Drive in the TCV and DIII-D tokamaks. *Phys. Rev. Lett.*, 88:205001, 2002.

[8] P. Nikkola, O. Sauter, R. Behn, S. Coda, I. Condrea, T. P. Goodman, M. A. Henderson, R. W. Harvey, and the TCV team. Modelling of the electron cyclotron current drive experiments in the TCV tokamak. *Nuclear Fusion*, 43(11):1343–1352, 2003.

[9] D. Choi, S. Coda, J. Decker, J. Cazabonne, and Y. Peysson. Study of suprathermal electron dynamics during ECCD using hard X-ray measurements in the TCV tokamak. *Plasma Physics and Controlled Fusion*, 2020.

[10] Y. Sarazin, V. Grandgirard, J. Abiteboul, S. Allfrey, X. Garbet, Ph. Ghendrih, G. Latu, A. Strugarek, and G. Dif-Pradalier. Large scale dynamics in flux driven gyrokinetic turbulence. *Nuclear Fusion*, 50(5):054004, 2010.

[11] T. Görler, X. Lapillonne, S. Brunner, T. Dannert, F. Jenko, S.K. Aghdam, P. Marcus, B.F. McMillan, F. Merz, O. Sauter, D. Told, and L. Villard. Flux- and gradient-driven global gyrokinetic simulation of tokamak turbulence. *Physics of Plasmas*, 18(5):056103, 2011.

[12] Y. Idomura. Full-f gyrokinetic simulation over a confinement time. *Physics of Plasmas*, 21(2):022517, 2014.

[13] E. Lanti, N. Ohana, N. Tronko, T. Hayward-Schneider, A. Bottino, B.F. McMillan, A. Mishchenko, A. Scheinberg, A. Biancalani, P. Angelino, S. Brunner, J. Dominski, P. Donnel, C. Gheller, R. Hatzky, A. Jocksch, S. Jolliet, Z.X. Lu, J.P. Martin Collar, I. Novikau, E. Sonnendrücker, T. Vernay, and L. Villard. Orb5: A global electromagnetic gyrokinetic code using the PIC approach in toroidal geometry. *Computer Physics Communications*, 251:107072, 2020.

[14] C. F. Kennel and F. Engelmann. Velocity space diffusion from weak plasma turbulence in a magnetic field. *The Physics of Fluids*, 9(12):2377–2388, 1966.

[15] I. Lerche. Quasilinear theory of resonant diffusion in a magneto-active, relativistic plasma. *The Physics of Fluids*, 11(8):1720–1727, 1968.

[16] R. Koch. Wave-particle interactions in plasmas. *Plasma Physics and Controlled Fusion*, 48(12B):B329–B345, 2006.

[17] Y. Peysson and J. Decker. Numerical simulations of the radio-frequency-driven toroidal current in tokamaks. *Fusion Science and Technology*, 65(1):22–42, 2014.

[18] J. Decker and Y. Peysson. DKE: A fast numerical solver for the 3-D relativistic bounce-averaged electron Drift Kinetic Equation. Technical report, EUR-CEA-FC-1736, 2004.

[19] T.H. Stix. *Waves in plasmas*. New York: American Institute of Physics, 1992.

[20] M. Bornatici, R. Cano, O. De Barbieri, and F. Engelmann. Electron cyclotron emission and absorption in fusion plasmas. *Nuclear Fusion*, 23(9):1153–1257, sep 1983.

[21] M Bornatici. Theory of electron cyclotron absorption of magnetized plasmas. *Plasma Physics*, 24(6):629–638, jun 1982.

[22] M. Bornatici, F. Engelmann, and G. G. Lister. Finite larmor radius effects in the absorption of electromagnetic waves around the electron cyclotron frequency. *The Physics of Fluids*, 22(9):1664–1666, 1979.

[23] Y. Peysson, J. Decker, and L. Morini. A versatile ray-tracing code for studying rf wave propagation in toroidal magnetized plasmas. *Plasma Physics and Controlled Fusion*, 54(4):045003, 2012.

[24] Antoine J. Cerfon and Jeffrey P. Freidberg. "one size fits all" analytic solutions to the grad–shafranov equation. *Physics of Plasmas*, 17(3):032502, 2010.

[25] X. Garbet, Y. Idomura, L. Villard, and T.H. Watanabe. Gyrokinetic simulations of turbulent transport. *Nuclear Fusion*, 50(4):043002, 2010.

[26] F. Castejón and S. Eguilior. Langevin equations for quasi-linear wave-particle interaction. *Plasma Physics and Controlled Fusion*, 45(2):159–167, 2003.

[27] P Donnel, C Gheller, S Brunner, L Villard, E Lanti, N Ohana, and M Murugappan. Moment approach of the multi-species non-linear coulomb collision operator adapted to particle-in-cell codes. *Plasma Physics and Controlled Fusion*, 63(2):025006, 2020.

[28] T. Görler, N. Tronko, W. A. Hornsby, A. Bottino, R. Kleiber, C. Norscini, V. Grandgirard, F. Jenko, and E. Sonnendrücker. Intercode comparison of gyrokinetic global electromagnetic modes. *Physics of Plasmas*, 23(7):072503, 2016.